The Astrophysical Journal, 843:21 (13pp), 2017 July 1 https://doi.org/10.3847/1538-4357/aa745e

Particle Acceleration during Magnetic Reconnection in a Low-beta Plasma

Xiaocan Li[1,2,3], Fan Guo[3], Hui Li[3], and Gang Li[1,2]
[1] Department of Space Science, University of Alabama in Huntsville, Huntsville, AL 35899, USA
[2] Center for Space Plasma and Aeronomic Research, University of Alabama in Huntsville, Huntsville, AL 35899, USA
[3] Los Alamos National Laboratory, Los Alamos, NM 87545, USA
Received 2017 January 30; revised 2017 May 3; accepted 2017 May 16; published 2017 June 27

Abstract

Magnetic reconnection is a primary mechanism for particle energization in space and astrophysical plasmas. By carrying out two-dimensional (2D) fully kinetic simulations, we study particle acceleration during magnetic reconnection in plasmas with different plasma β (the ratio between the thermal pressure and the magnetic pressure). For the high-β cases, we do not observe significant particle acceleration. In the low-β regime ($\beta < 0.1$), we find that reconnection is efficient at energizing both electrons and ions. While the distribution of accelerated particles integrated over the whole simulation box appears highly non-thermal, it is actually the superposition of a series of distributions in different sectors of a 2D magnetic island. Each of those distributions has only a small non-thermal component compared with its thermal core. By tracking a large number of particles, we show that particles get energized in *X*-line regions, contracting magnetic islands, and magnetic island coalescence regions. We obtain the particle energization rate $\boldsymbol{j} \cdot \boldsymbol{E}$ by averaging over particle drift motions and find that it agrees well with the particle kinetic energy change. We quantify the contribution of curvature drift, gradient drift, polarization drift, magnetization, non-gyrotropic effect, and parallel electric field in different acceleration regions. We find that the major energization is due to particle curvature drift along the motional electric field. The other particle motions contribute less but may become important in different acceleration regions. The highly efficient particle energization in low-β plasmas may help us understand the strong particle energization in solar flares and accretion disk coronae.

Key words: acceleration of particles – accretion, accretion disks – magnetic reconnection – Sun: corona – Sun: flares

1. Introduction

Magnetic reconnection rearranges the magnetic topology and converts the magnetic energy into plasma kinetic energy (Priest & Forbes 2000; Yamada et al. 2010). In space and astrophysical systems, reconnection is a primary driver of magnetic energy release and particle energization processes, leading to explosive phenomena (e.g., Zweibel & Yamada 2009). For example, solar flare observations have revealed an efficient energy release process with 10%–50% of the magnetic energy converted into plasma kinetic energy within 10^{2-3} s (Lin & Hudson 1976). Similar processes may occur in accretion systems. Rapid X-ray variability (milliseconds to seconds) indicates that the fast energy release in the accretion disk corona possibly occurs through a magnetic reconnection process (Galeev et al. 1979; Haardt et al. 1994). Magnetic reconnection heats plasma and may even accelerate particles to non-thermal energies. The non-thermal acceleration can be efficient in a low-β plasma ($\beta < 0.1$), with the free magnetic energy being much larger than the initial particle thermal energy. In particular, hard X-ray (HXR) observations by *Ramaty High Energy Solar Spectroscopic Imager* (*RHESSI*) suggest that a large fraction of electrons are non-thermal inside the HXR sources above the magnetic loops during solar flares (Krucker et al. 2010; Krucker & Battaglia 2014). The non-thermal electrons tend to develop into a power-law energy distribution that contains energy on the same order of the dissipated magnetic energy (Krucker et al. 2010; Krucker & Battaglia 2014; Oka et al. 2015). The acceleration of ions can be as efficient as that of electrons. This is evidenced by *RHESSI* observations of the correlation of electron-generated HXR flux and ion-generated γ-ray flux (Shih et al. 2009). Despite a wide range of observational evidence, how efficient non-thermal acceleration occurs in the reconnection layer is still a major unsolved problem in magnetic reconnection studies.

To study non-thermal particle acceleration during reconnection, a fully kinetic simulation is desirable, as it solves the evolution of particle distribution and electromagnetic fields self-consistently, including the feedback of accelerated particles to the fields. Most previous simulations have focused on reconnection in a plasma with relatively high β ($\beta > 0.1$), where the energization does not strongly modify the particle distribution function (Hoshino et al. 2001; Drake et al. 2006, 2010; Oka et al. 2010). Meanwhile, simulations of relativistic reconnection did show non-thermal distributions, but only within the localized *X*-region (Zenitani & Hoshino 2001), which is on the kinetic scale and cannot account for the observed particle acceleration. In the past few years, kinetic simulations (Guo et al. 2014; Melzani et al. 2014; Sironi & Spitkovsky 2014; Guo et al. 2015, 2016; Werner et al. 2016) have made significant progress in the magnetically dominated regime (magnetic energy $\gg$ plasma kinetic energy). These works found that particles over the entire reconnection region can develop a power-law energy distribution with a spectral index $1 < p < 2$, when the magnetization parameter $\sigma = B^2/(4\pi n_e m_e c^2) \gg 1$. Motivated by these results and the fact that plasmas are low-β ($\beta \ll 1$) but nonrelativistic in the solar corona (Gary 2001; Lin 2011) and the accretion disk corona (Galeev et al. 1979), Li et al. (2015) performed kinetic

simulations in a nonrelativistic low-β ($\beta \sim 0.01$) proton–electron plasma. When integrating the energy distribution over the whole simulation domain, it resembles a non-thermal spectrum. However, the local energy spectrum was not examined. One of the goals of this paper is to study the local particle energy distribution.

Earlier two-dimensional (2D) simulations have identified different acceleration mechanisms in various regions of the reconnection layer. Electrons get accelerated by a parallel electric field when they enter the reconnection region along the reconnection separatrix (Drake et al. 2005; Egedal et al. 2012, 2015). They are then accelerated by the reconnection electric field in the *X*-type region close to the reconnection point (Hoshino et al. 2001; Fu et al. 2006; Oka et al. 2010). These electrons are further accelerated by the reconnection electric field through particle curvature drift and gradient drift (Hoshino et al. 2001; Fu et al. 2006; Pritchett 2006; Oka et al. 2010). Drake et al. (2006) proposed a mechanism through which particles gain energy when they reflect from either end of contracting magnetic islands. This mechanism can accelerate electrons in a large portion of the reconnection region, as both modeling (Shibata & Tanuma 2001; Drake et al. 2006; Loureiro et al. 2007; Bhattacharjee et al. 2009; Daughton et al. 2009) and observations (Sheeley et al. 2004) suggest that reconnection in solar flares involves a large number of magnetic islands. Further simulations have shown that the merging regions between islands are also efficient at accelerating electrons via an anti-reconnection electric field (Oka et al. 2010; Le et al. 2012; Drake et al. 2013). Here, the important problem is identifying the main acceleration region and primary acceleration mechanism. Through tracking energetic electron trajectories, several works have suggested that the most energetic electrons are accelerated in the magnetic island-merging region (Oka et al. 2010; Nalewajko et al. 2015).

While tracking the particle orbits is useful for examining the basic acceleration process, it is difficult to infer the main energization process from a limited number of particle orbits. There have been several studies examining the energization processes by calculating the energization rate $\boldsymbol{j}\cdot\boldsymbol{E}$ and the contributions from different drift terms in the guiding center approximation (Dahlin et al. 2014; Guo et al. 2014, 2015; Li et al. 2015). Using this description, different simulations have all identified that the major acceleration mechanism is particle curvature drift along the electric field induced by the reconnection outflow. One of the goals of this paper is to study the acceleration processes in different acceleration regions and determine their relative importance not only though tracking particles but also through calculating the plasma energization rate. Additionally, those simulations with the $\boldsymbol{j}\cdot\boldsymbol{E}$ analysis focus on studying electron acceleration without addressing the ion acceleration. It is interesting to see whether electron energization and ion energization are similar.

In this paper, we perform 2D kinetic simulations of magnetic reconnection in a nonrelativistic proton–electron plasma with a range of plasma $\beta_e = \beta_i = 0.007 - 0.2$. This paper extends Li et al. (2015) on electron energization and studies ion energization as well. We focus on understanding the dependence of the energy conversion and particle energization on plasma β. The low-β condition is achieved by both increasing the magnetic field strength (or equivalently decreasing the particle density) and by decreasing the plasma temperature. By tracking a large number of particles, we identify the particle energization regions and energization patterns. In order to estimate the energization mechanisms, the energy change rate $\boldsymbol{j}\cdot\boldsymbol{E}$ through different drift terms is examined. We compare the energization mechanisms in reconnection outflow, contracting magnetic island and island-merging regions. We carry out similar analyses for ions to show differences and similarities between electron energization and ion energization. Section 2 describes the numerical methods and parameters. Section 3 describes simulation results. In Section 4, we present discussions and conclusions based on our simulation results.

2. Numerical Simulations

We carry out 2D kinetic simulations using the VPIC code, which solves Maxwell's equations and the Vlasov equation using the particle-in-cell method in a fully relativistic manner (Bowers et al. 2008). The initial configuration is a force-free current sheet with a magnetic field described as $\boldsymbol{B} = B_0\tanh(z/\lambda)\hat{x} + B_0\,\mathrm{sech}(z/\lambda)\hat{y}$, corresponding to a magnetic field with a uniform strength B_0 rotating by 180° across a layer with a half-thickness λ. We choose $\lambda = d_i$ in all simulations, where $d_i = c/\omega_{pi} = c/\sqrt{4\pi n_i e^2/m_i}$ is the ion inertial length. The plasma consists of protons and electrons with a mass ratio $m_i/m_e = 25$ for most cases, but a case with $m_i/m_e = 100$ is included to examine the effect of the mass ratio. The initial distributions for both electrons and protons are Maxwellian, with a uniform density n_0 and temperature $T_i = T_e = T_0$. A drift velocity for electrons U_e is added to represent the current density that satisfies the Ampere's law. The plasma $\beta = 2\beta_e = 16\pi n_0 kT_0/B_0^2$, where β_e is the electron plasma. We vary β_e by using different T_0 and/or B_0 in different simulations. Note that a change in B_0 will also result in a change of the Alfvén speed $v_A = B_0/\sqrt{4\pi n_0 m_i}$. The parameter values for all runs are listed in Table 1, which gives the asymptotic values of the magnetic field strength B_0, c/v_A, $c/v_{\rm the}$, ω_{pe}/Ω_{ce}, β_e, the grid sizes, and the number of particles per cell per species `nppc`. The domain sizes are $L_x \times L_z = 200d_i \times 100d_i$ for all simulations. For fields, we employ periodic boundaries along the *x*-direction and conducting boundaries along the *z*-direction. For particles, we employ periodic boundaries along the *x*-direction and reflect boundaries along the *z*-direction. We add a long-wavelength perturbation with $B_z = 0.03B_0$ to induce reconnection (Birn et al. 2001) for all runs except run R4, which starts from numerical noise generated by the random sampling of a finite number of particles.

3. Results

3.1. General Evolution

As reconnection starts, the current layer breaks into a series of magnetic islands, which merge with each other to form larger islands. The largest island in the system keeps growing until its size is comparable to the system size and at that time reconnection ceases. Figure 1(a) shows the evolution of the out-of-plane magnetic field B_y in run R1. About 10 small magnetic islands are generated from the initial current sheet. They interact and coalesce with each other, with three primary islands remaining at $t\Omega_{ci} = 152.5$. One of them is located at $x \sim 120d_i$, consisting of two smaller merging islands (pointed out by the arrow). As the islands move away from each other, the stretched current sheet at $x \sim 75$–$100d_i$ becomes unstable again and produces a secondary island (at $x \sim 90d_i$ in the

Table 1
List of Simulation Runs

Run	m_i/m_e	B_0	c/v_A	$c/v_{\rm the}$	ω_{pe}/Ω_{ce}	β_e	$N_x \times N_z$	nppc
R1	25	1.0	5.0	7.07	1.0	0.02	4096 × 2048	400
R2	25	$1/\sqrt{3}$	8.7	12.25	$\sqrt{3}$	0.02	4096 × 2048	200
R3	25	$1/\sqrt{10}$	15.8	22.36	$\sqrt{10}$	0.02	4096 × 2048	200
R4	25	1.0	5.0	7.07	1.0	0.02	4096 × 2048	200
R5	100	1.0	10.0	7.07	1.0	0.02	8000 × 4000	350
R6	25	$\sqrt{3}$	2.9	7.07	$1/\sqrt{3}$	0.007	4096 × 2048	200
R7	25	$1/\sqrt{3}$	8.7	7.07	$\sqrt{3}$	0.07	4096 × 2048	200
R8	25	$1/\sqrt{10}$	15.8	7.07	$\sqrt{10}$	0.2	4096 × 2048	400

Note. B_0 is the asymptotic magnetic field strength. $v_A = B_0/\sqrt{4\pi n_0 m_i}$ is the Alfvén speed of the inflow region. $v_{\rm the} = \sqrt{2kT_e/m_e}$ is the electron thermal speed. $\omega_{pe} = \sqrt{4\pi n_0 e^2/m_e}$ is the electron plasma frequency. $\Omega_{ce} = eB/(m_e c)$ is the electron gyrofrequency. $\beta_e = 8\pi n_0 kT_e/B_0^2$ is the electron plasma β. N_x and N_z are the grid sizes along the x-direction and z-direction, respectively. nppc is the number of particles per cell for each species. R4 is similar to R1, except there is no initial long-wavelength perturbation.

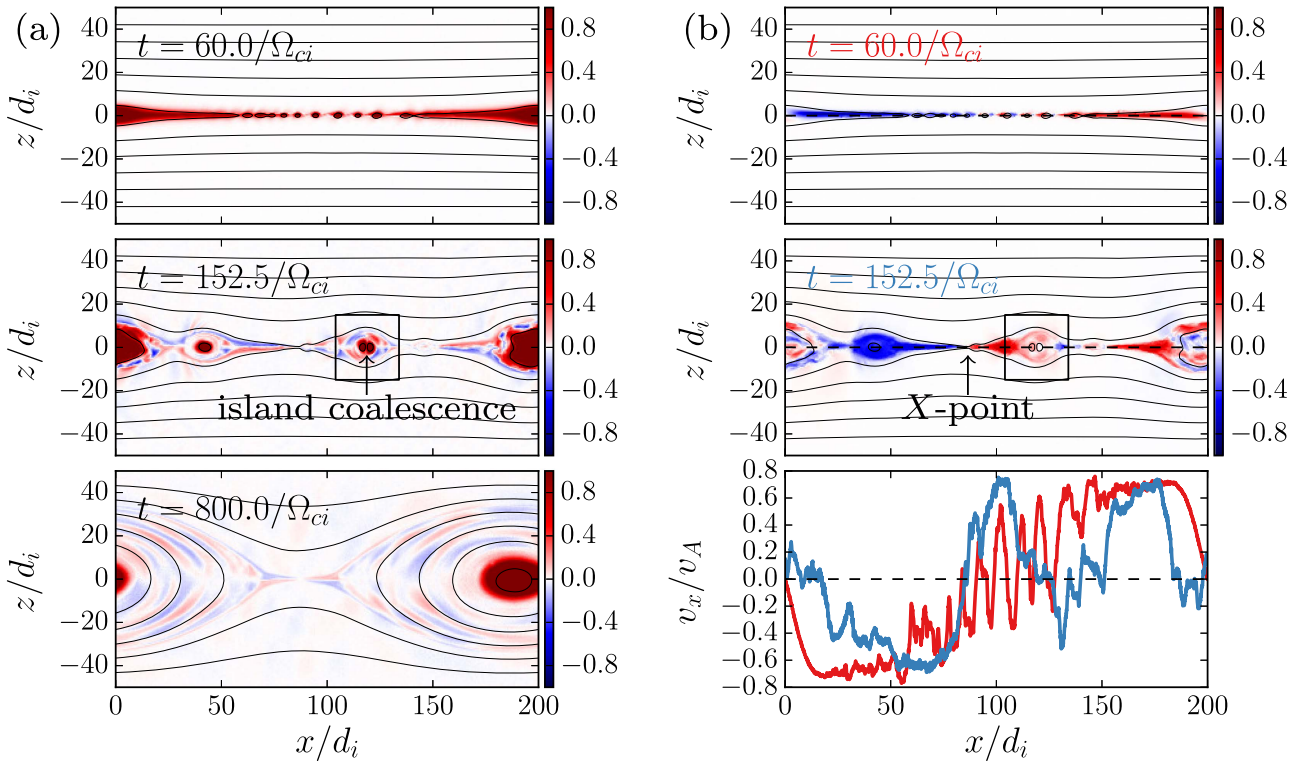

Figure 1. (a) Out-of-plane magnetic field B_y in run R1 at $t\Omega_{ci} = 60$, 152.5, and 800. The arrow in the middle panel indicates one representative island-merging region. (b) The bulk flow velocity in run R1 at $t\Omega_{ci} = 60$ and 152.5. The dashed lines in the upper two panels are a horizontal cut along $z = 0$. Plotted in the bottom panel is v_x along the cut. The red line is the cut at $t\Omega_{ci} = 60$. The blue line is the cut at $t\Omega_{ci} = 152.5$. v_x is normalized to the reconnection inflow Alfvén speed v_A. The overplotted arrow indicates a reconnection X-point, indicated by the bi-directional reconnection outflow.

middle panel). The magnetic flux of the guide field B_y is initially in the center of the force-free current sheet. As the current layer breaks into multiple magnetic islands, the magnetic flux of B_y gets convected into these islands. The current sheet then evolves like a Harris current sheet without a guide field (antiparallel reconnection). B_y at late time shows quadrupole structures (bottom two panels of Figure 1), which are a signature of Hall physics in antiparallel reconnection (Drake et al. 2008).

The reconnection process drives fast bulk flow in the x-direction. Figure 1(b) shows the fluid velocity v_x at $t\Omega_{ci} = 60$ and 152.5. v_x is the center-of-mass velocity by averaging over the fluid velocities of electrons and ions in a computing cell $v_x = \sum_s n_s m_s v_{sx}/\sum_s n_s m_s$. At $t\Omega_{ci} = 60$, the newly formed magnetic islands are strongly contracting. A cut along the x-direction shows that v_x varies between $0.5v_A$ and $-0.5v_A$ in $10d_i$. At $t\Omega_{ci} = 152.5$, the diverging flow (shown by the arrow) at $x \sim 85d_i$ indicates a reconnection X-point, and the converging flow at $x \sim 100$–$140d_i$ indicates a contracting magnetic island. Both regions can be efficient at accelerating particles, as we will discuss below.

3.2. Energy Evolution

We now consider the energy conversion for different runs. Figure 2(a) shows the time evolution of the magnetic energy ε_b, electric energy ε_e, electron kinetic energy K_e, and ion kinetic energy K_i in run R1 ($\beta_e = 0.02$). About 40% of the magnetic energy is converted into plasma kinetic energy. Electrons gain 4.8 times their initial energy, and ions gain 8.4 times their

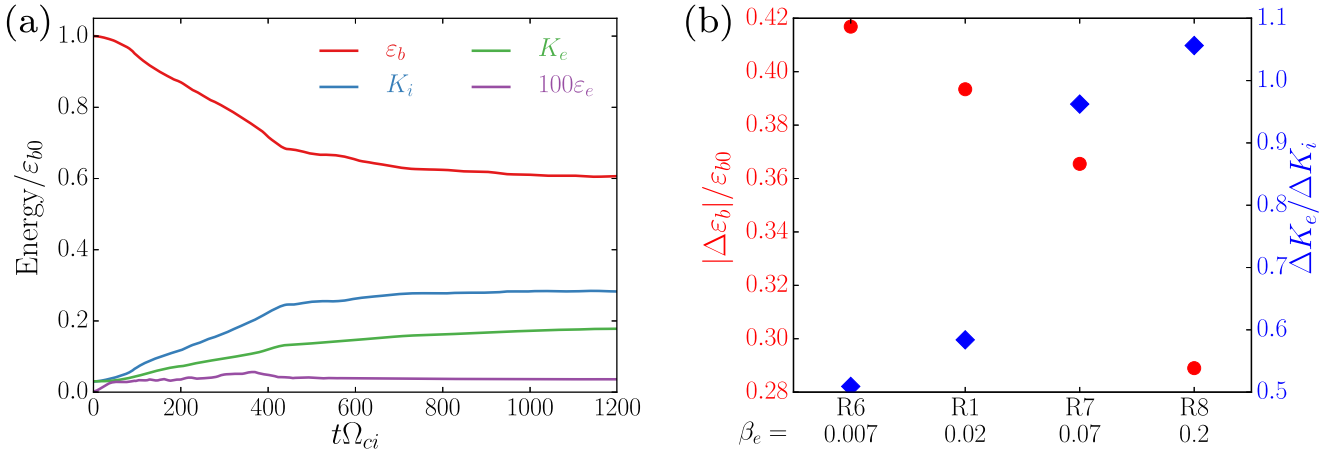

Figure 2. (a) The time evolution of the magnetic energy ε_b, electric energy ε_e, electron kinetic energy K_e, and ion kinetic energy K_i in run R1 ($\beta_e = 0.02$). They are normalized by the initial magnetic energy ε_{b0}. (b) The fraction of dissipated magnetic energy $\Delta\varepsilon_b/\varepsilon_{b0}$ (red dots) and the ratio of the electron energy gain ΔK_e and the ion energy gain ΔK_i (blue diamonds) for runs with different plasma β.

initial energy. Table 2 lists the fraction of dissipated magnetic energy $\Delta\varepsilon_b/\varepsilon_{b0}$, $\Delta K_e/K_{e0}$, and $\Delta K_i/K_{i0}$. We pick four runs and plot $\Delta\varepsilon_b/\varepsilon_{b0}$, $\Delta K_e/K_{e0}$, and $\Delta K_i/K_{i0}$ in Figure 2(b). These runs have the same initial particle energies, and the plasma β is varied through changing the initial magnetic field. We find that about 38% of magnetic energy get converted in R1 ($\beta_e = 0.02$), and the fraction increases to 42% in R6, with $\beta_e = 0.007$, but decreases to 29% in R8, with $\beta_e = 0.2$. This, combined with the fact that the ratio between magnetic field energy and kinetic energy is higher in the low-β runs, enables particles to gain more energy in plasma with lower-β. Table 2 shows that K_e increases by 57% in run R8 ($\beta_e = 0.2$). This is highly enhanced in run R6 ($\beta_e = 0.007$), where K_e increases 13.29 times. The plasma β also changes the energy partition between electrons and ions. The blue diamonds in Figure 2(b) show that the low-β reconnection is more efficient at energizing ions. $\Delta K_e/\Delta K_i > 1$ for R8 ($\beta_e = 0.2$), while the ratio decreases to 0.47 in run R6 ($\beta_e = 0.007$). The energy partition not only depends on the plasma β but also the plasma temperature and the mass ratio. Table 2 shows that $\Delta K_i/\Delta K_e$ decreases from 1.74 in R1 ($c/v_{\rm the} = 7.07$) to 1.06 in R3 ($c/v_{\rm the} = 22.36$). This result suggests that decreasing the plasma temperature yields stronger electron acceleration relative to ion acceleration. Table 2 also shows that the $\Delta K_i/\Delta K_e$ is larger in R5 ($m_i/m_e = 100$) than that in R1-R4 ($m_i/m_e = 25$), indicating that a higher mass ratio in simulations leads to stronger ion acceleration relative to electron acceleration.

Table 2
Energy Conversion for Different Runs

Run	$\lvert\Delta\varepsilon_b\rvert/\varepsilon_{b0}$	$\Delta K_e/K_{e0}$	$\Delta K_i/K_{i0}$
R1	0.39	4.85	8.43
R2	0.38	5.11	7.43
R3	0.37	6.22	6.59
R4	0.38	5.16	7.93
R5	0.38	4.09	8.82
R6	0.42	13.29	28.05
R7	0.36	2.21	2.29
R8	0.29	0.57	0.54

Note. $|\Delta\varepsilon_b|/\varepsilon_{b0}$ is the fraction of dissipated magnetic energy. ΔK_e and ΔK_i are the energy gain for electrons and ions, respectively. K_{e0} and K_{i0} are the initial energies of electrons and ions, respectively.

3.3. Particle Acceleration

Energy conversion during reconnection leads to efficient particle acceleration. Figure 3 shows the time evolution of particle energy spectra for both electrons and ions in runs R1 ($\beta_e = 0.02$) and R8 ($\beta_e = 0.2$). The embedded subpanels show the time evolution of maximum particle energies in corresponding cases. For run R1, the maximum electron energy is about 500 times larger than the initial thermal energy $\varepsilon_{\rm th}$, and the maximum ion energy is about $1500\varepsilon_{\rm th}$. In run R8 ($\beta_e = 0.2$), the energization is not as efficient as run R1. The maximum energy is about $40\varepsilon_{\rm th}$ for electrons and $80\varepsilon_{\rm th}$ for ions, an order of magnitude lower than that in run R1. Figure 3 shows that the final spectra for both runs deviate from the initial Maxwellian distribution (dashed curves). Compared to the results of R8 ($\beta_e = 0.2$), the final spectrum for run R1 ($\beta_e = 0.02$) has a much larger tail, and particles are accelerated into higher energies. The tail has a flat component from several to about 10 thermal energies, and for higher energy the spectrum is steeper and power-law-like, extending to several hundred thermal energies (see the discussion below).

The subpanels in Figure 3 show that the maximum particle energies saturate around $t\Omega_{ci} = 200$–400. A more detailed analysis shows that particles with the highest energy nestle inside the largest islands. During the late stage ($t\Omega_{ci} > 400$), these particles can hardly access any significant electric field when the islands interact with smaller ones. This is why the maximum particle energies saturate even though reconnection is still ongoing in these 2D simulations.

To study the non-thermal nature of the spectrum tail, we first plot the final energy spectra for all runs and for both electrons and ions in Figure 4. If one subtracts the low-energy thermal core (a Maxwellian distribution) to obtain the accelerated component, the accelerated distribution appears non-thermal for the low-β case. Figure 4 shows that the overall electron and ion distributions both have a significant high-energy tail in the low-β runs. Figures 4(a) and (c) show that the high-energy tails are more obvious in the low-β runs. Figures 4(b) and (d) show that the spectra are similar in shape for simulations in plasmas with the same $\beta_e = 0.02$. We further separate the magnetic islands into different sectors, which are based on the contour of A_y. Figure 5 shows the particle energy distributions in run R1

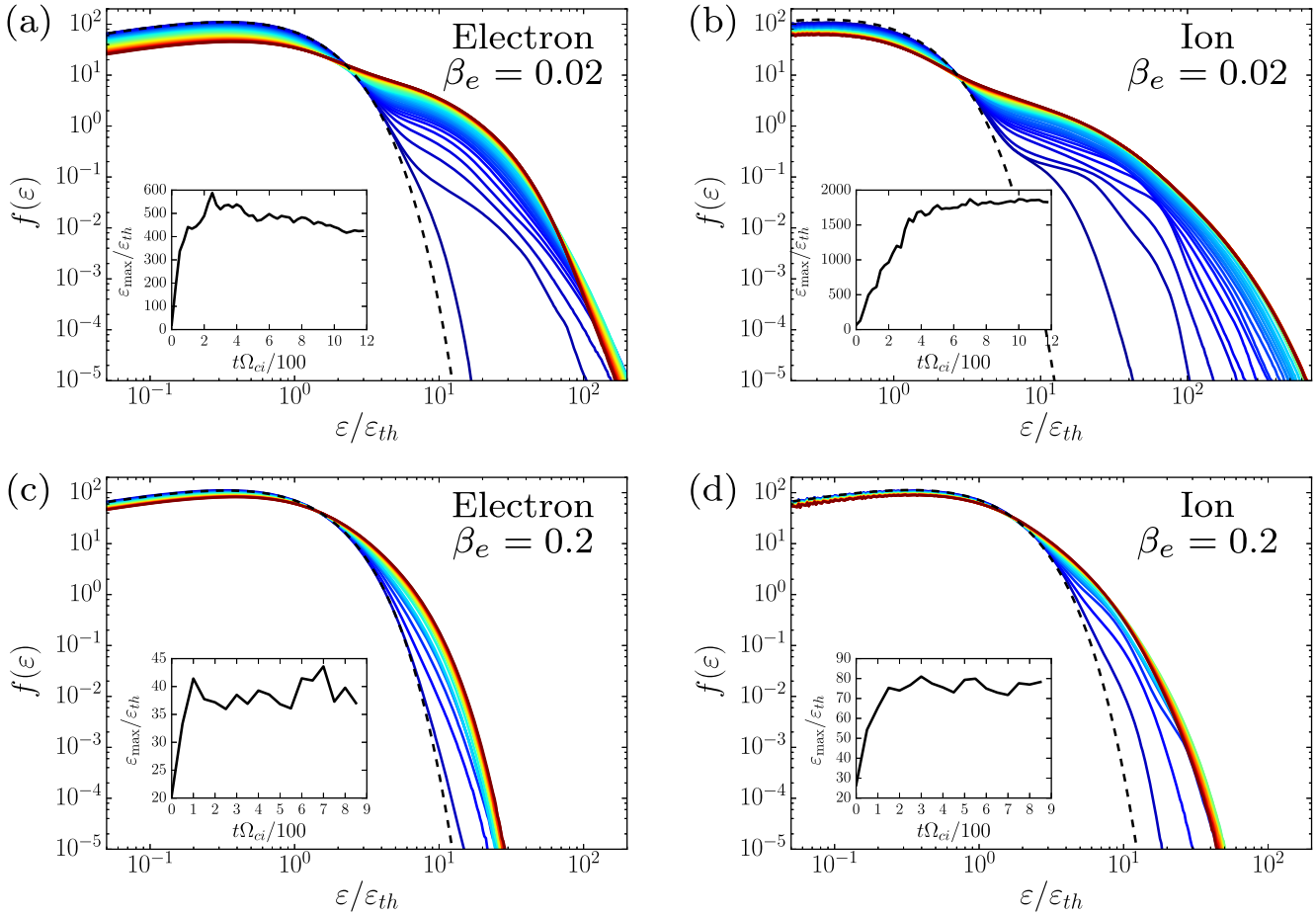

Figure 3. Time evolution of particle energy spectra for runs R1 and R8. The lines with different colors are particle spectra at different times. Curves are evenly spaced in time intervals of $t\Omega_{ci} = 25$ for R1 and $t\Omega_{ci} = 50$ for R8. The dashed line is the initial thermal distribution. The subpanels give the time evolution of the maximum energy ε_{max} normalized to the initial thermal energy ε_{th}. (a) Electron energy spectra for run R1. (b) Ion energy spectra for run R1. (c) Electron energy spectra for run R8. (d) Ion energy spectra for run R8.

($\beta_e = 0.02$) and R6 ($\beta_e = 0.007$). The first column shows the A_y contours. The region between the black solid lines indicates the reconnection region. The second and third columns show the electron and ion energy distributions, respectively. The overplotted dashed lines are the fitted Maxwellian distributions for the spectra in the center region of the magnetic island. While the overall electron distribution resembles a hard power-law distribution followed by a high-energy tail, Figures 5(b) and (e) show that the distribution in different sectors has a non-thermal tail that only contains about 1% of all electrons. The electron distributions in the inner sectors have higher temperatures than those in the outer sectors. This is because the electrons in the inner sectors of the magnetic island enter the reconnection region earlier and get accelerated more than the electrons in the outer sectors. In contrast to electrons, the ion spectrum in each sector is different from a single Maxwellian. This is because energetic ions have a much larger gyroradius ($\sim 10 d_i$ compared to $\sim d_i$ for energetic electrons), so ions in each sector are from a much broader region than the sector itself. To summarize, although the final spectra have highly non-thermal tails in the low-β runs, the spectra are actually a superposition of a series of distributions consisting of thermal and non-thermal components in different regions of the largest magnetic islands.

We track individual particles in run R1 to identify various particle acceleration regions. We choose three electrons that are energetic ($\varepsilon > 100\varepsilon_{th}$) by the end of run R1. Figures 6(a)–(c) show the trajectories of these electrons. Figure 6(d) shows the time evolution of their kinetic energies. $a_1 - a_3$, $b_1 - b_3$, and $c_1 - c_3$ indicate the acceleration phases for electrons a, b, and c, respectively. These electrons are accelerated in the X-line regions and then in the island regions. Most of the energization is associated with magnetic islands. We have identified a number of island-related processes that contribute differently for the acceleration of individual electrons: (1) island contraction, meaning that a particle gets accelerated by circulating a contracting magnetic island; (2) island-merging, meaning that the underlying particle is accelerated in the anti-reconnection electric field in merging islands; (3) island-trapping, indicating that a particle is trapped in one side of the moving island and keeps getting accelerated. The island contraction process is important for all electrons (phases a_2, $b_1 - b_3$, and c_1). It can account for most of the acceleration for electron b, and contribute significantly for the acceleration of electrons a and c. The island-merging process is important for electron a (phase a_1), but is negligible for electrons b and c. These results show that electron acceleration involves multiple mechanisms and that the major mechanism for each electron can be different.

Ion acceleration can be as complicated as electron acceleration. Figure 7 shows three ion trajectories in run R1. One difference between ion acceleration and electron acceleration is

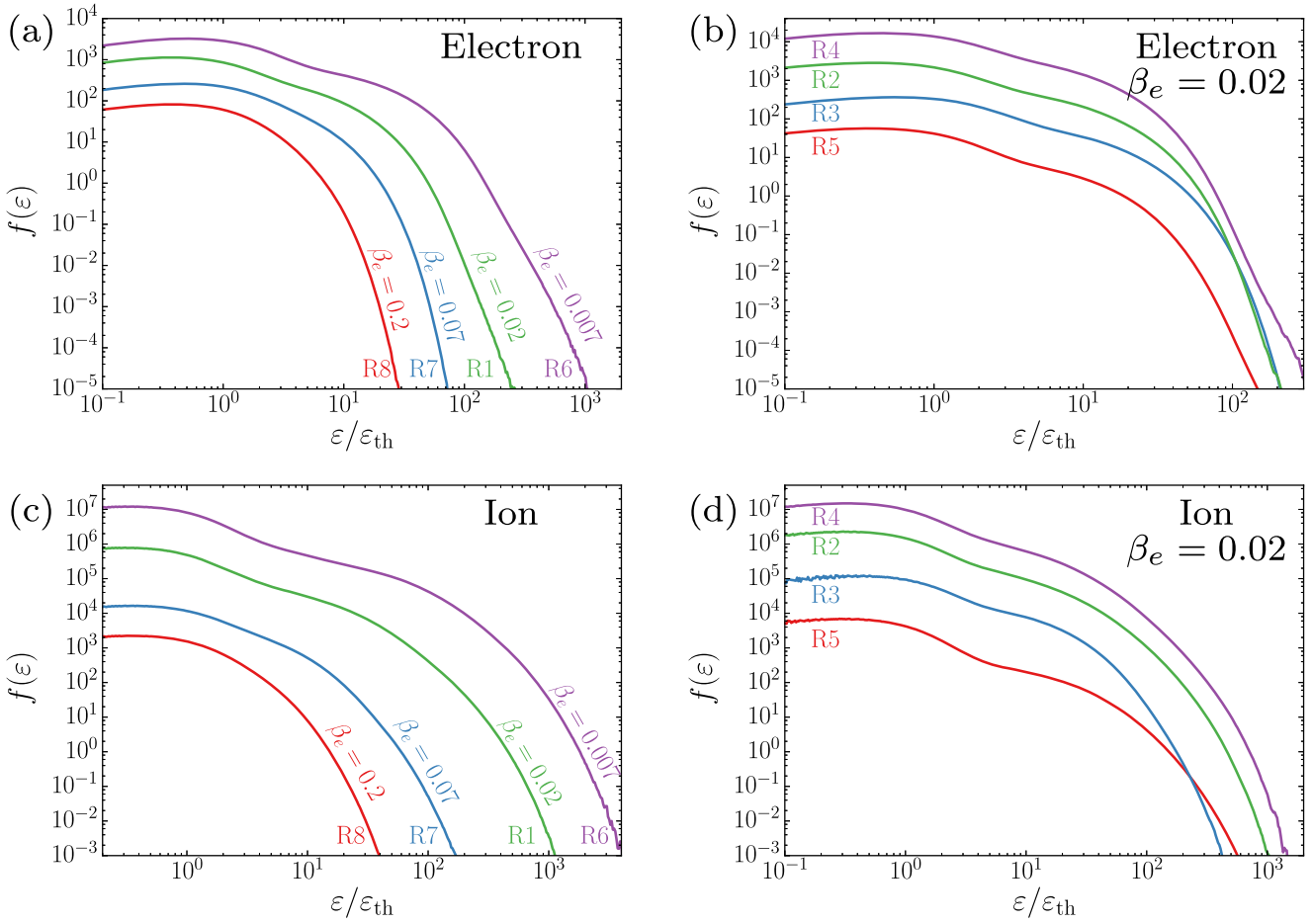

Figure 4. Particle energy spectra for different simulations. We normalize the kinetic energy ε to the initial thermal energy $\varepsilon_{\rm th}$, which is the same for both electrons and ions in our simulations. (a) Electron spectra for four runs with different plasma β ranging from $\beta_e = 0.007$ to 0.2. (b) Electron spectra for four runs with the same β, but different plasma temperatures. Among them, R5 has a different mass ratio $m_i/m_e = 100$. (c) Ion spectra for the four runs with different plasma β. (d) Ion spectra for the four runs with the same plasma β but different plasma temperature. The spectra are shifted along the y-axis to separate different runs.

that ions have a fast energy gain phase when they enter the reconnection region. The ions gain energy $\sim 0.5 m_i v_A^2 \sim 0.02 m_i c^2$ during this process. For example, ion a enters the reconnection region at $x \sim 90 d_i$ and then moves to $x \sim 100 d_i$ without a whole gyromotion. Its energy gradually increases (top panel of (d)) and the ion drifts along the positive y-direction during this period. The three ions are different from each other in their following acceleration processes. Ion a gets further accelerated in two contracting islands (phase a_2 and a_3). Ion b gains most of its energy when it drifts along E_y in an island-merging region during $t\Omega_{ci} = 250$–300. Ion c gains most its energy through bouncing back and forth inside a single contracting island. The complicated ion trajectories make it difficult to identify the major acceleration mechanisms.

3.4. Particle Energization in Different Regions

Examining particle trajectories can help identify various acceleration regions, but the fact that we can only carefully analyze a small number of them makes it difficult to determine the energization mechanisms. To statistically study the particle energization process, we calculate macroscopic quantities that represent the energy gain by different types of particle motions.

The plasma energization is through the work done by the electric force on the particles $\varepsilon_c \equiv \int\int_0^{t_0} \boldsymbol{j}_s \cdot \boldsymbol{E} dt d^3\boldsymbol{r}$, where $\boldsymbol{j}_s$ is the current density due to the motion of a single particle species, and $\boldsymbol{E}$ is the electric field. For a single particle species, the parallel and perpendicular current densities are

$$\boldsymbol{j}_{s\parallel} = q_s n_s \boldsymbol{v}_{s\parallel}, \quad \boldsymbol{j}_{s\perp} = q_s n_s \boldsymbol{v}_{s\perp}, \tag{1}$$

where q_s is the particle charge, n_s is the particle number density, and $\boldsymbol{v}_{s\parallel}$ and $\boldsymbol{v}_{s\perp}$ are averaged velocities parallel and perpendicular with respect to the local magnetic field direction, respectively. We define the particle energization rate $\dot{\varepsilon}_c$ as $\int \boldsymbol{j}_s \cdot \boldsymbol{E} d^3\boldsymbol{r}$. Then, $\int \boldsymbol{j}_{s\parallel} \cdot \boldsymbol{E}_\parallel d^3\boldsymbol{r}$ is the particle energization produced by the parallel electric field, and $\int \boldsymbol{j}_{s\perp} \cdot \boldsymbol{E}_\perp d^3\boldsymbol{r}$ is the particle energization produced by the perpendicular electric field. Figure 8 shows $\dot{\varepsilon}_c$ for both electrons and ions in run R1. The particle energization by $\boldsymbol{E}_\perp$ is dominant for both electrons and ions, although the energization by $\boldsymbol{E}_\parallel$ is comparable with that by $\boldsymbol{E}_\perp$ for electrons at the beginning of the simulation. Toward the end of the simulation, $\int \boldsymbol{j}_{s\perp} \cdot \boldsymbol{E}_\perp d^3\boldsymbol{r}$ yields over 80% of both electron energization and ion energization in run R1. The fraction is similar for all the other runs, as shown in Tables 3 (for electrons) and 4 (for ions), indicating that the plasma energization is preferentially produced by the perpendicular electric field. From the point of view of a single particle, it gains most of its energy when it moves along(for ions)/against(for electrons) the perpendicular electric field. In the

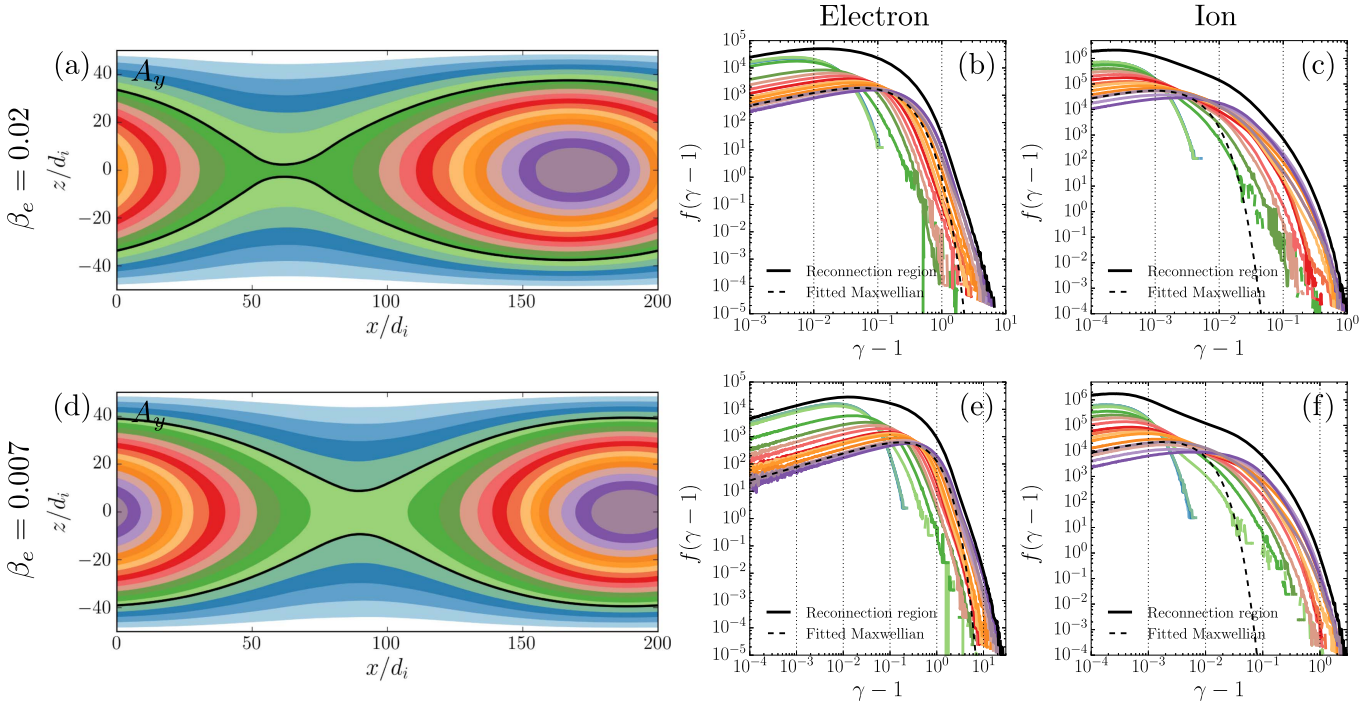

Figure 5. Particle energy spectra in different sectors. (a) The contour of the out-of-plane component of the vector potential A_y in run R1 ($\beta_e = 0.02$). The region between the black lines indicates the reconnection region. (b) Electron energy spectra in different sectors, with colors indicated in (a). (c) Ion energy spectra in different sectors. The solid black lines are the spectra in the reconnection region between the black lines indicated in (a). The dashed black lines are the fitted Maxwellian distributions for the spectra in the center region of the magnetic island. (d) The contour of the out-of-plane component of the vector potential A_y in run R6 ($\beta_e = 0.007$). (e) and (f) are the same as (b) and (c), except they are for run R6.

following discussions, we use the perpendicular current densities raised from different particle motions to study the energization processes from different types of particle motions.

For a well-magnetized particle (gyroradius $\ll$ field variation scale), single particle motion can be well represented by its gyromotion and different types of drift motion. The initial force-free magnetic field configuration has a guide-field component in the center of the current sheet. This guarantees that the magnetic field is not weak in the diffusion regions during the major reconnection events ($t\Omega_{ci} < 50$). In our low-β simulations, the gyroradius is much smaller than the inertial lengths (e.g., $r_e/d_e = v_{\rm the}\omega_{pe}/(c\Omega_{ce}) = \sqrt{\beta_e/2} < 0.2$), and therefore the electron pressure agyrotropy (the measure of deviation from the guiding center description) is close to zero, except for close to the diffusion region (see Figure 3(b) in Li et al. 2015), so the electrons are well-magnetized in reconnection exhausts and magnetic islands. By averaging these drift motions over a large number of electrons, we can construct the perpendicular current density $\boldsymbol{j}'_{s\perp}$ for electrons as

$$\boldsymbol{j}'_{s\perp} = \boldsymbol{j}_c + \boldsymbol{j}_g + \boldsymbol{j}_p + \boldsymbol{j}_{\boldsymbol{E}\times\boldsymbol{B}} + \boldsymbol{j}_m, \tag{2}$$

where $\boldsymbol{j}_c$ is due to curvature drift, $\boldsymbol{j}_g$ is due to gradient drift, $\boldsymbol{j}_p$ is due to polarization drift, and $\boldsymbol{j}_{\boldsymbol{E}\times\boldsymbol{B}}$ is due to $\boldsymbol{E}\times\boldsymbol{B}$ drift. We include one more term, $\boldsymbol{j}_m$, which is the magnetization current and is due to particle gyromotion (Parker 1957). The expressions of these current densities are

$$\boldsymbol{j}_c = p_{\parallel s}\frac{\boldsymbol{B}\times(\boldsymbol{B}\cdot\nabla)\boldsymbol{B}}{B^4}, \tag{3}$$

$$\boldsymbol{j}_g = p_{\perp s}\left(\frac{\boldsymbol{B}}{B^3}\right)\times\nabla B, \tag{4}$$

$$\boldsymbol{j}_p = n_s m_s \frac{\boldsymbol{B}}{B^2}\times\frac{d\boldsymbol{u}_s}{dt}, \tag{5}$$

$$\boldsymbol{j}_m = -\left[\nabla\times\frac{p_{\perp s}\boldsymbol{B}}{B^2}\right]_\perp. \tag{6}$$

Where $p_{\parallel s}$ and $p_{\perp s}$ are parallel and perpendicular pressure with respect to the local magnetic field; n_s is the particle species number density; m_s is the particle mass; and $\boldsymbol{u}_s$ is the fluid velocity. We calculate $p_{\parallel s}$, $p_{\perp s}$, and $\boldsymbol{u}_s$ using the particle distribution f_s in each computational cell. $p_{\parallel s} \equiv m_s\int f_s v_{\parallel s}^2 d^3\boldsymbol{v}_s$, $p_{\perp s} \equiv 0.5 m_s\int f_s v_{\perp s}^2 d^3\boldsymbol{v}_s$, and $\boldsymbol{u}_s \equiv \int f_s \boldsymbol{v}_s d^3\boldsymbol{v}_s/n_s$. For simplicity, we will neglect the subscript s in the following discussions unless otherwise specified. We define an additional current density as

$$\boldsymbol{j}_a \equiv -\frac{1}{B^2}[\nabla\cdot(\mathbf{P} - p_\perp\mathbf{I} - (p_\parallel - p_\perp)\hat{\boldsymbol{b}}\hat{\boldsymbol{b}})]\times\boldsymbol{B}, \tag{7}$$

where $\mathbf{P} \equiv \int m\boldsymbol{v}\boldsymbol{v}f d^3\boldsymbol{v}$ is the full pressure tensor; $p_\perp\mathbf{I} + (p_\parallel - p_\perp)\hat{\boldsymbol{b}}\hat{\boldsymbol{b}}$ is the gyrotropic pressure tensor, which is a good approximation of $\mathbf{P}$ if particles are well-magnetized. In the reconnection region, the magnetic field can be small and the particles can be energetic, so $\boldsymbol{j}_a$ is defined to measure the effect of a non-gyrotropic pressure tensor in regions where particles are not well-magnetized

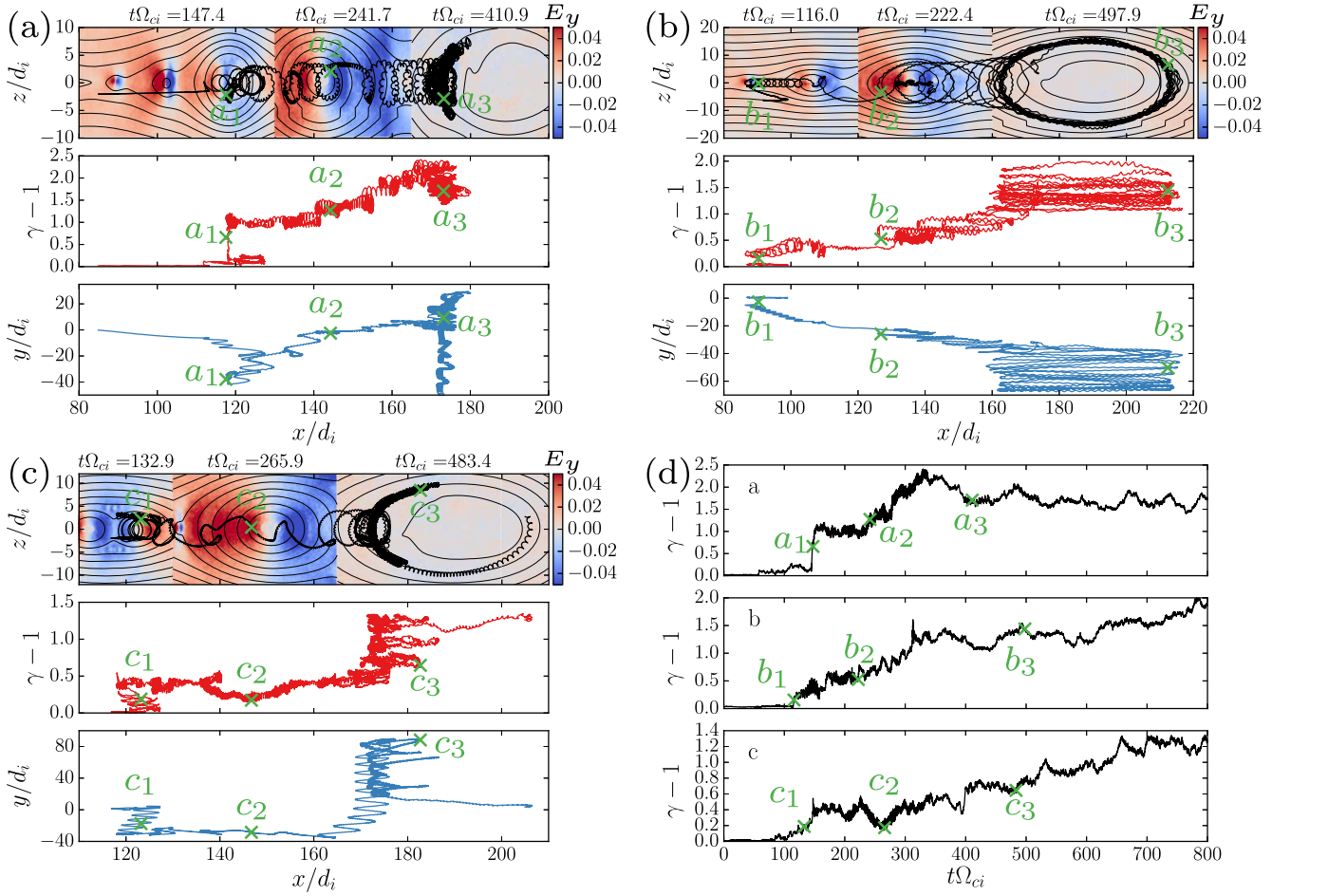

Figure 6. Three typical electron trajectories in run R1. The top panels of (a)–(c) show the trajectories in the simulation x–z plane. The background is the out-of-plane electric field E_y. We plot E_y at three time frames: $a_1 - a_3$ for electron a, $b_1 - b_3$ for electron b , and $c_1 - c_3$ for electron c. The green crosses are the particle positions at these time frames. The middle panels of (a)–(c) show the electron energy evolution with its x position. The bottom panels show the electron's y position vs. its x position. We calculate the y position by integrating v_y over time. Because particles can cross the right boundary and come back from the left boundary due to the periodic boundary condition, we shift the leftmost trajectory points to the right. (d) The time evolution of the electron kinetic energy for the three electrons plotted in (a)–(c).

Figure 9 shows the particle energization rate $\dot{\varepsilon}_c$ for electrons (top panel) and ions (bottom panel) through curvature drift (red), gradient drift (blue), and magnetization (green) in run R1. Particles gain energy by curvature drift and lose energy through gradient drift. The net effect is an energization since $\int \boldsymbol{j}_\perp'' \cdot \boldsymbol{E} d^3\boldsymbol{r} > 0$ (purple lines in Figure 9), where $\boldsymbol{j}_\perp''$ is the summation of these three terms. Note that $\int \boldsymbol{j}_\perp'' \cdot \boldsymbol{E} d^3\boldsymbol{r}$ matches well with the energy change rate for both electrons ($\dot{K}_e$) and ions ($\dot{K}_i$), which validates our drift-current analysis for low-β reconnection. We summarize the contributions of different drift motion to the particle energization for all 8 runs in Table 3 (electrons) and Table 4 (ions). For all runs, the particle energization through curvature drift ($\boldsymbol{j}_c$) is the dominant term, and the energization through gradient drift ($\boldsymbol{j}_g$) is negative. The other terms are generally smaller than these two terms but can become significant in some cases. For example, the particle energization through polarization drift ($\boldsymbol{j}_p$) contributes 14%–42% to the ion energy gain, which is much larger than that to the electron energy gain because $\boldsymbol{j}_p \sim m_s$. We find that $\int \boldsymbol{j}_a \cdot \boldsymbol{E} d^3\boldsymbol{r}$ is small for electrons in all runs, indicating that most electrons are well-magnetized. For ions, $\int \boldsymbol{j}_a \cdot \boldsymbol{E} d^3\boldsymbol{r}$ can lead up to 25% of the total energization for the worst cases with high plasma beta and weak magnetic field.

Using the drift analysis, we also study the plasma energization in local regions shown in the trajectory plots (Figures 6 and 7). Figure 10 shows the particle energization through different kinds of electric current in one reconnection exhaust ($150d_i < x < 185d_i$) for both electrons (left) and ions (right) in run R1 at $t\Omega_{ci} = 137.5$. The top two rows plot the 2D contour of different terms. The bottom row is the accumulation of the top rows along the x-direction, e.g., $\int_{x_0}^{x}\int_{z_{\min}}^{z_{\max}} \boldsymbol{j}_c \cdot \boldsymbol{E} dx dz$. For both electrons and ions, the energization close to the diffusion region ($x \sim 150d_i$) is negligible compared with that in the reconnection exhaust. The energizations through curvature drift (red) and gradient drift (blue) are the largest among all these terms, and the other terms are small compared to these two terms. The particle energization through curvature drift is positive because $\boldsymbol{j}_c \cdot \boldsymbol{E} \approx (p_\parallel \boldsymbol{B} \times \boldsymbol{\kappa}/B^2) \cdot (-\boldsymbol{u} \times \boldsymbol{B}) > 0$ when $\boldsymbol{u}$ and $\boldsymbol{\kappa}$ are along the same direction. The particle energization through gradient drift is negative because $\boldsymbol{j}_g \cdot \boldsymbol{E} \approx (p_\perp/B^3)(\boldsymbol{B} \times \nabla B) \cdot (-\boldsymbol{u} \times \boldsymbol{B}) < 0$ when $\boldsymbol{B} \times \nabla B$ and $-\boldsymbol{u} \times \boldsymbol{B}$ are along the opposite directions. Both terms peak in the center of the exhaust where the both the magnetic field line

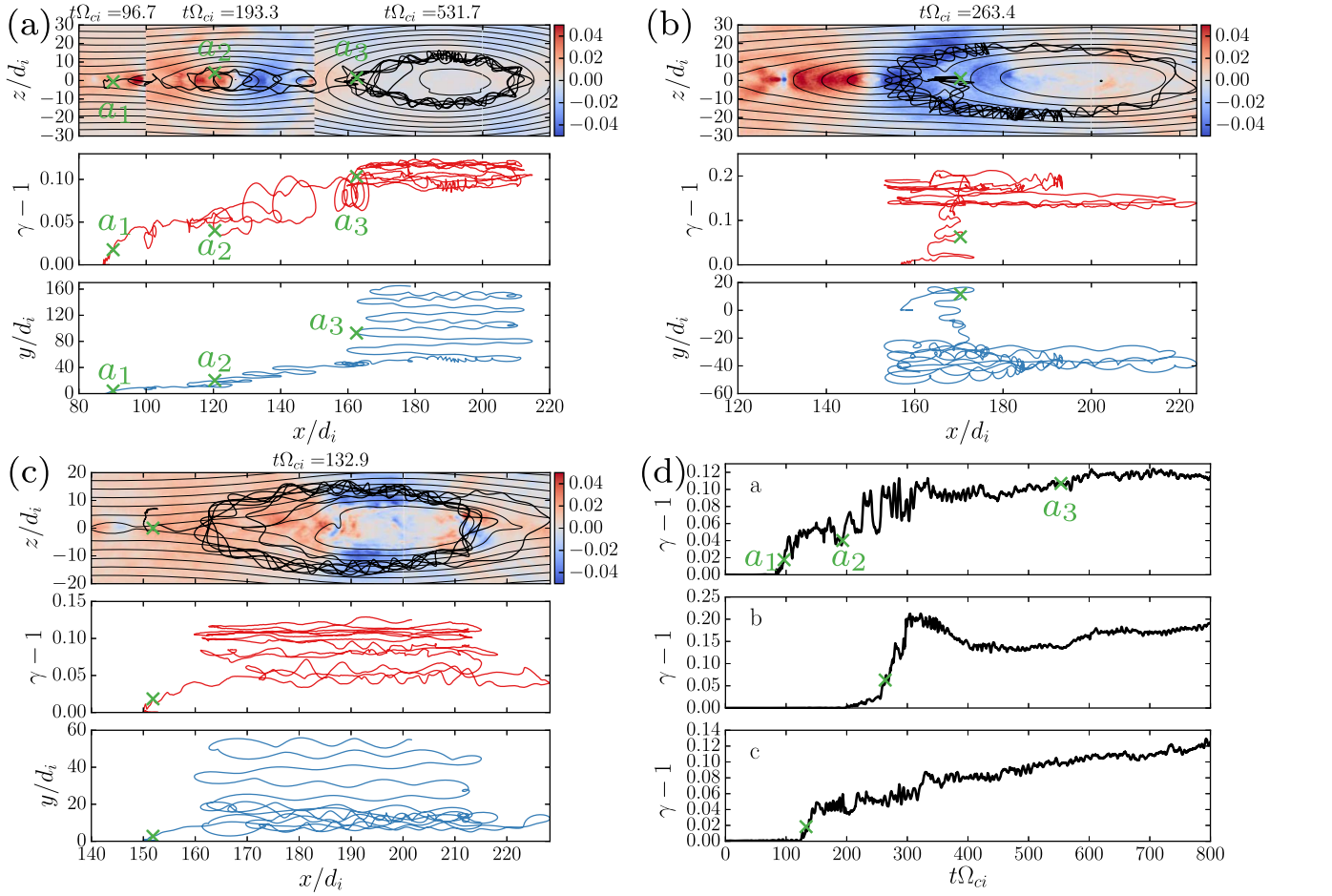

Figure 7. Three ion trajectories in run R1. The plots are similar to electrons in Figure 6. (a) One ion has three phases of acceleration. The plots in (b) and (c) are similar except that only one acceleration phase is marked. (d) The time evolution of the ion kinetic energy $\gamma - 1$ for these ions.

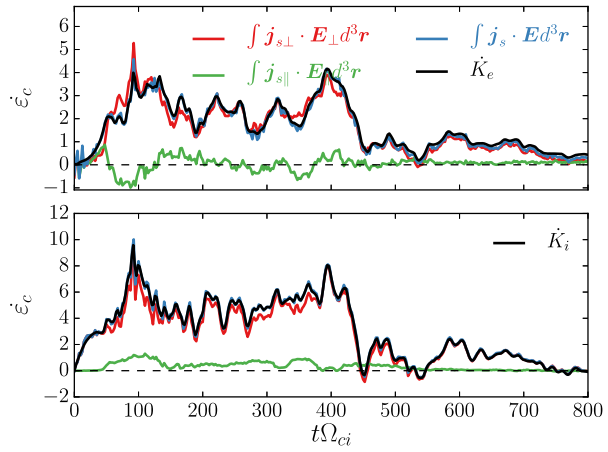

Figure 8. Particle energization rate $\dot{\varepsilon}_c$ by parallel electric field $\int \boldsymbol{j}_{s\parallel} \cdot \boldsymbol{E}_\parallel d^3\boldsymbol{r}$, perpendicular electric field $\int \boldsymbol{j}_{s\perp} \cdot \boldsymbol{E}_\perp d^3\boldsymbol{r}$, and total electric field $\int \boldsymbol{j}_s \cdot \boldsymbol{E} d^3\boldsymbol{r}$ for electrons (top) and ions (bottom). $\dot{K}_e$ and $\dot{K}_i$ are the energy change rates for electrons and ions. The plotted quantities are spatial integrals over the entire simulation box, and they are normalized by $m_e c^2 \omega_{pe}$.

curvature κ and ∇B are the largest. The accumulation lines in the bottom row show that $\boldsymbol{j}_c \cdot \boldsymbol{E}$ is larger than $\boldsymbol{j}_g \cdot \boldsymbol{E}$, so particles can gain energy when passing through this reconnection exhaust.

Figure 11 shows the particle energization in a region where two magnetic islands are merging (square box in Figure 1). A current sheet forms at $x \sim 117 d_i$ along the z-direction by the antiparallel B_z shown in Figure 12. Both $\boldsymbol{j}_c \cdot \boldsymbol{E}$ and $\boldsymbol{j}_g \cdot \boldsymbol{E}$ are still the largest among these terms, suggesting that the curvature drift gives strong acceleration in the island-merging region. The particle energization through polarization drift ($\boldsymbol{j}_p \cdot \boldsymbol{E}$) is comparable with these two terms for ions, because the flow is decelerated along the z-direction at $x \sim 117$–$120 d_i$. Figure 12 shows that the closed field lines containing the two small islands block the bulk flow v_z at $z \sim -5 d_i$ and $5 d_i$. The particle energization by a parallel electric field ($\boldsymbol{j}_\parallel \cdot \boldsymbol{E}$) is comparable with the largest two terms for electrons, because there is a guide field during this reconnection event since B_y is finite in both magnetic islands (see Figure 12). This result is consistent with previous efficient parallel acceleration in a guide-field reconnection (Dahlin et al. 2014; Wang et al. 2016). Last but not least, $\boldsymbol{j}_a \cdot \boldsymbol{E}$ is comparable with the largest two terms, indicating that particles are not well-magnetized in this region. This is because pre-accelerated energetic particles have large gyroradius, yielding "meandering-type" crossing orbits (Stanier et al. 2015), during which ions cross the island-merging region multiple times without a complete gyromotion (see the green cross region in the top panel of Figure 7(b)). This result suggests that the "meandering-type" crossing orbits can enhance particle energization in the island-merging regions.

As the two islands are merging, the newly formed large island is contracting, as indicated by the opposite v_x at the two sides of this island in Figure 12. This contracting island is also efficient at accelerating particles. The major particle energization

Table 3
Particle Energization ε_c due to Different Currents for Electrons

Run	$\boldsymbol{j}_{\parallel}\cdot\boldsymbol{E}$	$\boldsymbol{j}_{\perp}\cdot\boldsymbol{E}$	$\boldsymbol{j}'_{\perp}\cdot\boldsymbol{E}$	$\boldsymbol{j}_c\cdot\boldsymbol{E}$	$\boldsymbol{j}_m\cdot\boldsymbol{E}$	$\boldsymbol{j}_g\cdot\boldsymbol{E}$	$\boldsymbol{j}_p\cdot\boldsymbol{E}$	$\boldsymbol{j}_a\cdot\boldsymbol{E}$
R1	0.10	0.81	0.77	1.51	−0.30	−0.58	0.04	0.10
R2	0.03	0.87	0.74	1.39	0.05	−0.80	0.03	0.07
R3	0.10	0.69	0.61	1.45	−0.20	−0.72	0.03	0.05
R4	0.11	0.85	0.82	1.28	−0.10	−0.53	0.04	0.13
R5	0.02	0.82	0.84	1.75	−0.03	−1.02	0.02	0.12
R6	0.04	0.87	0.98	1.34	−0.04	−0.52	0.06	0.14
R7	0.02	0.74	0.63	1.63	0.01	−1.12	0.02	0.09
R8	−0.08	0.73	0.43	2.43	−0.36	−1.70	0.03	0.03

Note. The results are the ratios of different terms to ΔK_e, e.g., $\int \boldsymbol{j}_c\cdot\boldsymbol{E}d^3\boldsymbol{r}dt/\Delta K_e$. $\boldsymbol{j}_{\parallel}$ is due to parallel electron motion. $\boldsymbol{j}_{\perp}$ is due to perpendicular electron motion. $\boldsymbol{j}_c$ is due to curvature drift. $\boldsymbol{j}_m$ is due to the magnetization. $\boldsymbol{j}_g$ is due to gradient B drift. $\boldsymbol{j}_p$ is due to polarization drift. $\boldsymbol{j}_a$ is due to the agyrotropic pressure tensor. $\boldsymbol{j}'_{\perp}=\boldsymbol{j}_c+\boldsymbol{j}_m+\boldsymbol{j}_g+\boldsymbol{j}_p+\boldsymbol{j}_a$. The subscript is neglected for simplicity.

Table 4
Particle Energization ε_c due to Different Currents for Ions

Run	$\boldsymbol{j}_{\parallel}\cdot\boldsymbol{E}$	$\boldsymbol{j}_{\perp}\cdot\boldsymbol{E}$	$\boldsymbol{j}'_{\perp}\cdot\boldsymbol{E}$	$\boldsymbol{j}_c\cdot\boldsymbol{E}$	$\boldsymbol{j}_m\cdot\boldsymbol{E}$	$\boldsymbol{j}_g\cdot\boldsymbol{E}$	$\boldsymbol{j}_p\cdot\boldsymbol{E}$	$\boldsymbol{j}_a\cdot\boldsymbol{E}$
R1	0.10	0.91	0.88	1.78	−0.31	−0.70	0.17	−0.06
R2	0.10	0.92	0.99	1.74	0.15	−1.04	0.20	−0.06
R3	0.08	1.00	1.19	2.11	−0.15	−0.98	0.42	−0.21
R4	0.10	0.92	0.87	1.72	−0.08	−0.89	0.14	−0.02
R5	0.10	0.90	0.94	1.93	0.03	−1.14	0.24	−0.02
R6	0.12	0.91	0.99	1.47	−0.01	−0.60	0.16	−0.03
R7	0.10	0.94	0.97	2.30	0.13	−1.54	0.26	−0.18
R8	0.04	1.00	0.90	3.54	−0.28	−2.29	0.18	−0.25

Note. The results are the ratios of different terms to ΔK_i, e.g., $\int \boldsymbol{j}_c\cdot\boldsymbol{E}d^3\boldsymbol{r}dt/\Delta K_i$. $\boldsymbol{j}_{\parallel}$ is due to parallel ion motion. $\boldsymbol{j}_{\perp}$ is due to perpendicular ion motion. $\boldsymbol{j}_c$ is due to curvature drift. $\boldsymbol{j}_m$ is due to the magnetization. $\boldsymbol{j}_g$ is due to gradient B drift. $\boldsymbol{j}_p$ is due to polarization drift. $\boldsymbol{j}_a$ is due to the agyrotropic pressure tensor. $\boldsymbol{j}'_{\perp}=\boldsymbol{j}_c+\boldsymbol{j}_m+\boldsymbol{j}_g+\boldsymbol{j}_p+\boldsymbol{j}_a$ The subscript is neglected for simplicity.

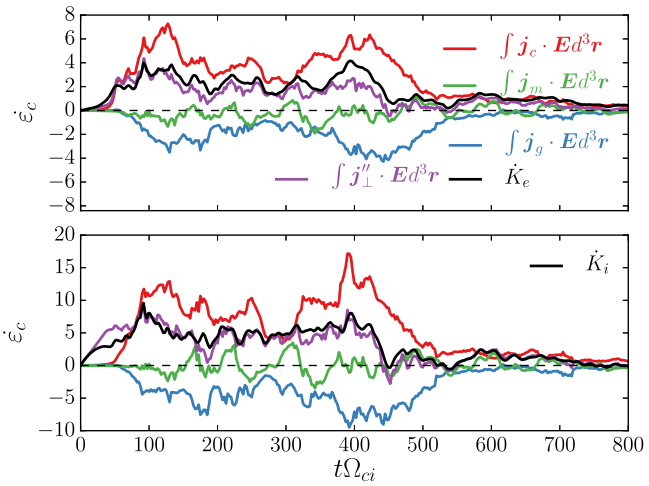

Figure 9. Particle energization due to different drift currents for electrons (top) and ions (bottom) for run R1. $\boldsymbol{j}_c$ is due to particle curvature drift. $\boldsymbol{j}_g$ is due to particle ∇B drift. $\boldsymbol{j}_m$ is due to magnetization. $\boldsymbol{j}''_{\perp}\equiv\boldsymbol{j}_c+\boldsymbol{j}_g+\boldsymbol{j}_m$, which does not include the current densities due to particle polarization drift and agyrotropic pressure tensor. $\dot{K}_e$ and $\dot{K}_i$ are the energy change rates for electrons and ions, respectively. They are all normalized by $m_e c^2\omega_{pe}$.

is through curvature drift, gradient drift, and polarization drift (for ions only). The energization through gradient drift is positive in thee regions because $\boldsymbol{j}_g\cdot\boldsymbol{E}>0$, as ∇B is along the same direction with $\boldsymbol{u}$. The ion energization through polarization drift is strong because the bulk flow is decelerated in this region.

4. Discussion and Conclusions

Particle acceleration is a central topic in space physics and astrophysics. In this work, we perform a series of 2D kinetic simulations to examine the energization of both electrons and ions during magnetic reconnection in a nonrelativistic plasma with β_e and β_i ranging from 0.007 to 0.2.

During reconnection, magnetic energy gets converted into plasma kinetic energy. We find that the particle energization is more efficient in low-β reconnection than in high-β reconnection, and that the energy partition between electrons and ions depends on plasma β, plasma temperature, and the proton and electron mass ratio. The energy conversion in the low-β regime drives strong particle energization. Both electrons and ions are energized to hundreds of times the initial thermal energy. The energized particles over the whole simulation box comprise a distribution with a high-energy tail. The high-energy tail of the electron distribution becomes harder as β gets lower. Through separating the final magnetic island into different sectors, we find that the accelerated electron distribution is actually a superposition of a series of different distributions, but each distribution only has a small non-thermal component relative to its thermal component. The distinct distributions in different sectors may be because the magnetic island in 2D reconnection confines electrons to different sectors. In a realistic 3D system, the closed magnetic island does not exist anymore, and the magnetic field lines become chaotic, which enables the mixing of particles originating from different regions and potentially leads to local particle distributions with stronger non-thermal components.

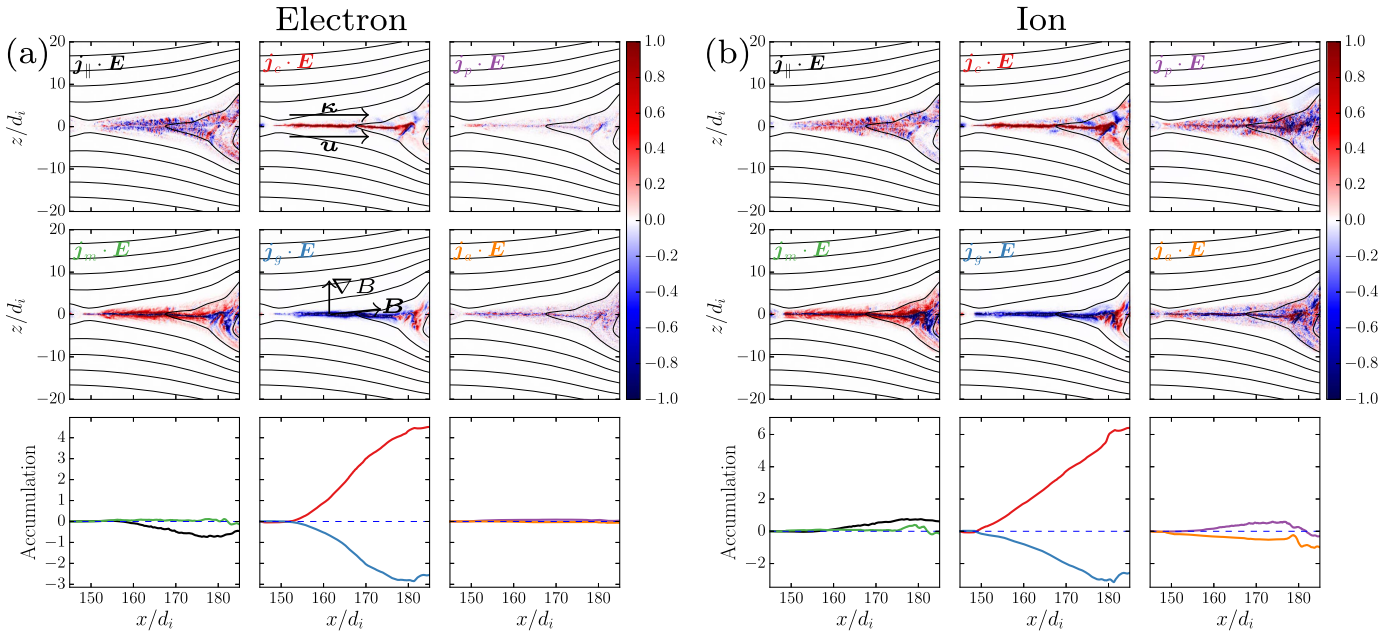

Figure 10. Particle energization in the reconnection exhaust for run R1 at $t\Omega_{ci} = 137.5$ for (a) electrons and (b) ions. The top two rows plot the 2D contours of different terms. They are normalized by $0.1en_0v_A^2B_0$. The bottom row is the accumulation of the top rows along the x-direction, e.g., $\int_{x_0}^{x}\int_{z_{\min}}^{z_{\max}} \boldsymbol{j}_c \cdot \boldsymbol{E}dxdz$. Overplotted are the directions of magnetic curvature $\boldsymbol{\kappa}$, bulk flow velocity $\boldsymbol{u}$, ∇B, and the magnetic field $\boldsymbol{B}$.

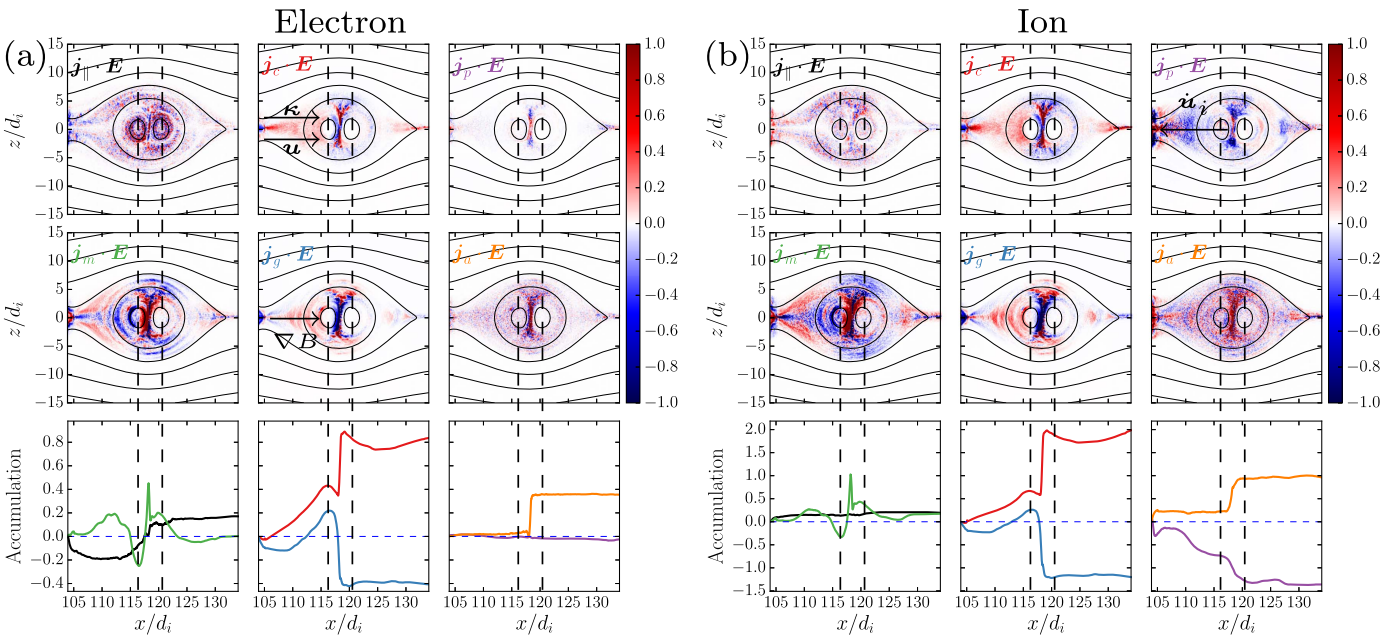

Figure 11. Particle energization in an island-merging region (between the dashed lines) for run R1 at $t\Omega_{ci} = 152.5$ for (a) electrons and (b) ions. Overplotted arrows are the direction of magnetic field curvature $\boldsymbol{\kappa}$, the bulk flow $\boldsymbol{u}$, the gradient of magnetic field ∇B, and the acceleration of the ion flow.

We find that the major energization occurs in reconnection exhausts and magnetic islands. We identify three important types of island-related acceleration processes as island contraction (a particle circles in the contracting island), island-merging (a particle accelerates in between merging islands), and island-trapping (a particle trapped in one end of a moving island). The current study has also included particle energization in the diffusion region. A magnetic field pile-up region is not specifically studied, but the drift approximation can be directly used to study it. This may be included in a future work. Protons are different from electrons in that they gain energy quickly when they enter the reconnection region and get "picked-up" by the Alfvénic reconnection outflow. This pre-acceleration process can lead to faster acceleration in island regions, since the energy gain through drift motion is proportional to the particle energy. For our analysis on using the drift approximation, we only focused on the total energization. This, however, does not capture the effect of pre-acceleration very well.

By studying the particle energization processes using a drift-current analysis, we find that over 80% of the particle energization is done by the perpendicular electric field. We construct $\boldsymbol{j}_\perp$ by averaging the particle drift motions and studying the particle energization by the perpendicular electric

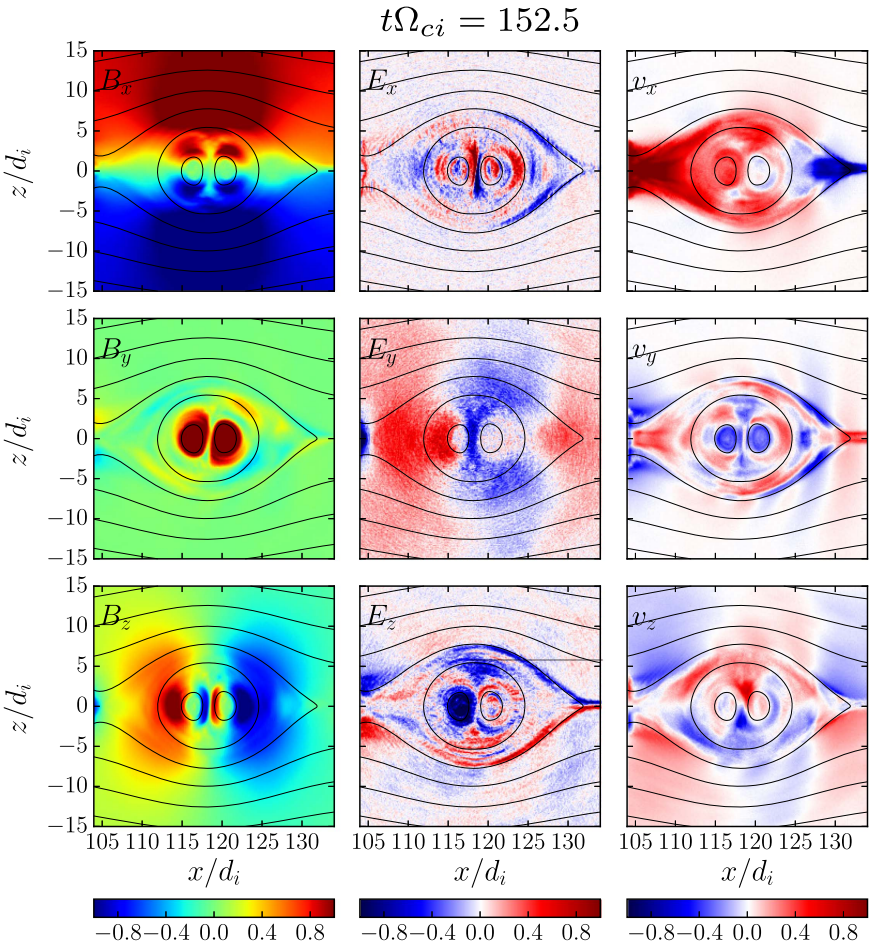

Figure 12. Electric field, magnetic field, and flow velocity at $t\Omega_{ci} = 152.5$, corresponding to Figure 11. The magnetic field is normalized by B_0. The electric field is normalized by $v_A B_0$. The velocity is normalized by $v_A/2$.

field. The major particle energization mechanism is through particle curvature drift along the electric field induced by the reconnection outflow in the reconnection exhausts, at the two sides of contracting magnetic islands and in the island-merging regions. The gradient drift gives non-negligible deceleration in the reconnection exhausts and island-merging regions but significant acceleration at the two sides of contracting magnetic islands. The polarization drift is negligible for electrons due to their small mass, but is significant for ions, especially in contracting islands and island-merging regions. We also find that the meandering particle orbits enhance energization in the island-merging regions.

The analysis using $\boldsymbol{j} \cdot \boldsymbol{E}$ is the total plasma energization, so it cannot differentiate heating from non-thermal particle energization. An alternative method is to calculate individual particle drift velocity $\boldsymbol{v}_d$ and energization $q\boldsymbol{v}_d \cdot \boldsymbol{E}$. Our preliminary results show that the sum of $q\boldsymbol{v}_d \cdot \boldsymbol{E}$ over the simulation box gives the same result as the sum of $\boldsymbol{j} \cdot \boldsymbol{E}$. The advantage of this method is that we could separate particles with different energies and hence differentiate the heating process and non-thermal acceleration process. We defer this to a future work.

Note that the study here focuses on particle energization at kinetic scales, which are usually much smaller than the observable scales. To explain the large-scale observations, we need to build a particle acceleration model based on the kinetic physics. Then, we can study particle energization through test-particle simulations (Zhou et al. 2015; Valle et al. 2016) or by solving particle transport equations (Parker 1965; Drake et al 2013; Zank et al. 2014; Le Roux 2015). Our preliminary results show that the particle drifts can be included in the compressional effects, and we can solve the Parker's transport equation coupled with MHD simulations to explain the large-scale acceleration during solar flares. We defer these results to a future publication.

In summary, we find that magnetic reconnection in nonrelativistic low-β proton–electron plasma is highly efficient at energizing both electrons and ions into high energies. The accelerated particles develop significant high-energy tails. In contrast, we do not observe significant particle energization in the high-β simulations. The particle distribution is a superposition of a series of thermal-like particle distributions in different sectors of the largest magnetic island in the simulations. Through tracking particles, we find that island contraction, island-merging, and particle-trapping are the major energization mechanisms. By calculating the particle energization, we find that the major energization mechanism is through particle curvature drift along the motional electric field. Particle gradient B drift yields particle deceleration in general and particle acceleration in contracting islands in particular.

Polarization drift yields ion cooling in contracting islands and island-merging regions. The meandering trajectories can enhance particle acceleration in the island-merging regions.

This work was supported by NASA Headquarters under the NASA Earth and Space Science Fellowship Program-Grant NNX13AM30H. F.G. was supported by NASA grant NNH16AC60I. We gratefully acknowledge our discussions with James Drake, Joel Dahlin, Jaehong Park, and Damiano Caprioli. We also acknowledgment the support by the DOE through the LDRD program at LANL. Simulations were performed with LANL institutional computing and also at the National Energy Research Scientific Computing Center.

References

Bhattacharjee, A., Huang, Y.-M., Yang, H., & Rogers, B. 2009, PhPl, 16, 112102
Birn, J., Drake, J. F., Shay, M. A., et al. 2001, JGR, 106, 3715
Bowers, K. J., Albright, B. J., Yin, L., Bergen, B., & Kwan, T. J. T. 2008, PhPl, 15, 055703
Dahlin, J. T., Drake, J. F., & Swisdak, M. 2014, PhPl, 21, 092304
Daughton, W., Roytershteyn, V., Albright, B. J., et al. 2009, PhRvL, 103, 065004
del Valle, M. V., de Gouveia Dal Pino, E. M., & Kowal, G. 2016, MNRAS, 463, 4331
Drake, J. F., Opher, M., Swisdak, M., & Chamoun, J. N. 2010, ApJ, 709, 963
Drake, J. F., Shay, M. A., & Swisdak, M. 2008, PhPl, 15, 042306
Drake, J. F., Shay, M. A., Thongthai, W., & Swisdak, M. 2005, PhRvL, 94, 095001
Drake, J. F., Swisdak, M., Che, H., & Shay, M. A. 2006, Natur, 443, 553
Drake, J. F., Swisdak, M., & Fermo, R. 2013, ApJL, 763, L5
Egedal, J., Daughton, W., & Le, A. 2012, NatPh, 8, 321
Egedal, J., Daughton, W., Le, A., & Borg, A. L. 2015, PhPl, 22, 101208
Fu, X. R., Lu, Q. M., & Wang, S. 2006, PhPl, 13, 012309
Galeev, A. A., Rosner, R., & Vaiana, G. S. 1979, ApJ, 229, 318
Gary, G. A. 2001, SoPh, 203, 71
Guo, F., Li, H., Daughton, W., & Liu, Y.-H. 2014, PhRvL, 113, 155005
Guo, F., Li, X., Li, H., et al. 2016, ApJL, 818, L9
Guo, F., Liu, Y.-H., Daughton, W., & Li, H. 2015, ApJ, 806, 167
Haardt, F., Maraschi, L., & Ghisellini, G. 1994, ApJ, 432, L95
Hoshino, M., Mukai, T., Terasawa, T., & Shinohara, I. 2001, JGR, 106, 25979
Krucker, S., & Battaglia, M. 2014, ApJ, 780, 107
Krucker, S., Hudson, H. S., Glesener, L., et al. 2010, ApJ, 714, 1108
Le, A., Karimabadi, H., Egedal, J., Roytershteyn, V., & Daughton, W. 2012, PhPl, 19, 072120
Le Roux, J. A., Zank, G. P., Webb, G. M., & Khabarova, O. 2015, Apj, 801, 112
Li, X., Guo, F., Li, H., & Li, G. 2015, ApJL, 811, L24
Lin, R. P. 2011, SSRv, 159, 421
Lin, R. P., & Hudson, H. S. 1976, SoPh, 50, 153
Loureiro, N. F., Schekochihin, A. A., & Cowley, S. C. 2007, PhPl, 14, 100703
Melzani, M., Walder, R., Folini, D., Winisdoerffer, C., & Favre, J. M. 2014, A&A, 570, A112
Nalewajko, K., Uzdensky, D. A., Cerutti, B., Werner, G. R., & Begelman, M. C. 2015, ApJ, 815, 101
Oka, M., Krucker, S., Hudson, H. S., & Saint-Hilaire, P. 2015, ApJ, 799, 129
Oka, M., Phan, T.-D., Krucker, S., Fujimoto, M., & Shinohara, I. 2010, ApJ, 714, 915
Parker, E. N. 1957, PhRv, 107, 924
Parker, E. N. 1965, P&SS, 13, 9
Priest, E., & Forbes, T. 2000, Magnetic Reconnection (Cambridge, CA: Cambridge Univ. Press)
Pritchett, P. L. 2006, JGRA, 111, 10212
Sheeley, N. R., Jr., Warren, H. P., & Wang, Y.-M. 2004, ApJ, 616, 1224
Shibata, K., & Tanuma, S. 2001, EP&S, 53, 473
Shih, A. Y., Lin, R. P., & Smith, D. M. 2009, ApJL, 698, L152
Sironi, L., & Spitkovsky, A. 2014, ApJL, 783, L21
Stanier, A., Daughton, W., Chacón, L., et al. 2015, PhRvL, 115, 175004
Wang, H., Lu, Q., Huang, C., & Wang, S. 2016, ApJ, 821, 84
Werner, G. R., Uzdensky, D. A., Cerutti, B., Nalewajko, K., & Begelman, M. C. 2016, ApJL, 816, L8
Yamada, M., Kulsrud, R., & Ji, H. 2010, RvMP, 82, 603
Zank, G. P., le Roux, J. A., Webb, G. M., Dosch, A., & Khabarova, O. 2014, ApJ, 797, 28
Zenitani, S., & Hoshino, M. 2001, ApJL, 562, L63
Zhou, X., Büchner, J., Bárta, M., Gan, W., & Liu, S. 2015, ApJ, 815, 6
Zweibel, E. G., & Yamada, M. 2009, ARA&A, 47, 291